Investigating flood processes in karst catchments by combining concentration-discharge relationship analysis and lateral flow simulation

Martin Le Mesnil, Jean-Baptiste Charlier, Roger Moussa, Yvan Caballero

1 # Investigating flood processes in karst catchments by combining
2 # Concentration-Discharge relationship analysis and lateral flow
3 # simulation

Martin Le Mesnil[1,2,3], Jean-Baptiste Charlier[1,2], Roger Moussa[3] and Yvan Caballero[1,2]

[1] BRGM, Univ. Montpellier, Montpellier, France.

[2] G-eau, INRAE, CIRAD, IRD, AgroParisTech, Supagro, BRGM, Montpellier, France.

[3] LISAH, Univ. Montpellier, INRAE, IRD, Montpellier SupAgro, Montpellier, France.

Corresponding author: Martin Le Mesnil (martin.lemesnil@gmail.com)

4

5

6 # 1 Introduction

7 Runoff at the catchment outlet has different origins depending on the water flow paths in

8 the surface, subsurface, and underground compartments. The joint study of hydrological and

9 hydrochemical signals through concentration-discharge (C-Q) relationships can help improving

10 our understanding of these origins and associated hydrological processes. Depending on the

11 context and nature of investigations, C-Q relationship analysis can be applied to different

12 variables, the most frequently monitored parameters being major ions or continuous physico-

13 chemical variables such as electrical conductivity, turbidity, alkalinity, or pH (e.g. Rose, 2003).

14 A synthesis by Knapp et al. (2020), based on results obtained in a Swiss mountainous catchment,

15   summarizes the main environmental drivers of C-Q relationships at the storm-event and longer

16   time scales. The main approaches encountered in the literature for the study of these

17   relationships are end-member mixing analysis (Burns et al., 2001; Doctor et al., 2006), statistical

18   approaches (Anderson et al., 1997) and hysteresis studies (Evans and Davies, 1998; Evans et al.,

19   1999; Rose, 2003; Rose et al., 2018). They led to advances in the understanding of aquifer

20   recharge and vulnerability (House and Warwick, 1998; Huebsch et al., 2014), streamflow

21   contributions (Ribolzi et al., 2000), and storm-event spring discharge (Toran and Reisch, 2012).

22   Most C-Q analyses are interpreted in terms of a two-component system involving pre-event

23   water (PEW) and event water (EW) (Evans et al., 1999; Rose, 2003), or include a third

24   component defined as soil or rapid infiltration water (Evans and Davies, 1998; Ribolzi et al.,

25   2000, Burns et al., 2001; Toran and Reisch, 2012). While most C-Q studies use the concentration

26   values of different streamflow source to perform the hydrograph separation, some use an *a priori*

27   separation to infer source concentration values (Neira et al., 2020).

28   At the catchment scale, hysteresis analyses allow studying C-Q relationships, using C and

29   Q data at a given monitoring station. Hysteresis loops are mainly characterized using

30   classifications of loop shapes, such as the widely used 6-type proposed by Evans and Davies

31   (1998), or more recent 9-type ones (Butturini et al., 2008; Heathwaite and Bieroza, 2020) using

32   hysteresis indices (see a synthesis by Lloyd et al., 2016). These approaches make it possible to

33   investigate streamflow contributions during storm events, knowing concentration ranking of

34   supposed end-members (Rose, 2003; Vaughan et al., 2017). When monitoring several gauging

35   stations for Q and C along the stream, it is possible to assess C-Q relationship spatial variability

36   at nested catchment scale. It is also possible to characterize it based on a reach scale approach

2

37   (between two gauging stations). In that case, water origin and flood hydrological processes can

38   be investigated by analyzing lateral exchanges, i.e. stream water gains or losses from or to

39   groundwater. Such analyses were performed by Covino et al. (2011) and Mallard et al. (2014),

40   using artificial tracing experiments to investigate stream composition changes. Analytical

41   approaches also exist, such as the advection-diffusion equation (ADE), widely used to model

42   conservative solute transport (Runkel, 1996; Baeumer et al., 2001; Hauns et al., 2001; Luhmann

43   et al., 2012). This equation is mathematically similar to the diffusive wave equation (DWE) and

44   both can be resolved using the Hayami analytical solution (1951), making it possible to simulate

45   lateral flows Q and C (Cholet et al., 2017).

46   Karst catchments are located in carbonate areas (including limestone and dolomite) and

47   cover 20% of Europe land surface and 35 % in France (Goldscheider et al., 2020). They are

48   known to be complex permeable hydrosystems, involving high rainfall infiltration rates through

49   open conduits and promoting fast groundwater flow and significant surface water-groundwater

50   interaction (Bakalowicz, 2005). In such areas, electrical conductivity (EC) provides information

51   on groundwater residence time and water origin, as it is controlled by bicarbonate, calcium, and

52   magnesium concentrations resulting from carbonate rock dissolution (Hess and White, 1988;

53   Lambán et al., 2015; Liu et al., 2007). Because EC can be easily monitored at high-frequency

54   time steps, it is a useful variable for the characterization of C-Q relationships, particularly in

55   karst catchments. Indeed, the contrast between water end-members is notable: low-

56   mineralization EW from surface runoff or fast groundwater flow, and high-mineralization PEW

57   from groundwater present in the aquifer prior to the storm event. The range of EC values is

58   variable, depending on groundwater residence time or mixing with fast rainwater infiltration, and

59   allow identifying PEW and EW occurrence. In the particular case of karst catchments, an

60   additional challenge is to distinguish EW from direct surface runoff on low permeability areas

61   and EW from fast infiltration in open conduits feeding rivers through springs (Hartmann et al.,

62   2021). Moreover, unexpected EC variations can occur during high-flow periods, as groundwater

63   boundaries extend and incorporate areas with different EC values (Ravbar et al., 2011).

64   Various methodologies have been used to explore EC-Q relationships during storm

65   events in karst catchments. Early studies mainly describe EC variations during storm events, an

66   EC drop being interpreted as an increasing EW contribution in streamflow, and complex

67   fluctuations corresponding to several simultaneous karst conduit contributions (Hess and White,

68   1988). Statistically-based methods exist, such as EC frequency distribution analysis (Massei et

69   al., 2007) which makes it possible to investigate the relative contributions of surface water and

70   groundwater to streamflow and how they are influenced by hydrological conditions.

71   Characterization of EC-Q hysteresis loops is also used, which makes it possible to study delays

72   between discharge and solute concentration variations, bringing to light the changing

73   hydrological processes at the scale of a storm event, or between different events (Fournier et al.,

74   2007; Toran and Reisch, 2012). Hysteresis loops of hydrographs at different locations within a

75   karst catchment were also studied to identify hydrological flows at nested catchment scale

76   (Zhang et al., 2020). Analysis of EC and Q patterns at the storm-event time scale have also

77   highlighted the importance of seasonal variability in the physico-chemical response of a karstic

78   spring (Fournier et al., 2007). Recently, EC-Q relationships at the reach scale were studied by

79   Cholet et al. (2017) using lateral exchange modeling to investigate conduit-matrix relationship

80   variability during storm events according to seasons. Each methodology helps better

4

81   understanding hydrological processes, and we identify a strong interest in combining different

82   approaches and to investigate both nested and reach scales to improve the conceptual model of

83   karst catchments.

84   The aim of this article is to assess the potential of a combined approach to investigate the

85   spatio-temporal variability of flood processes within karst catchments. To do that, we combine

86   two spatial scales of investigation: at the nested catchment scale, a classification of C-Q

87   hysteresis loops adapted to EC measurement in karst context; at the reach scale, an inverse

88   modeling of lateral flow Q and C. Using this combined approach, we will define what can be

89   learned from C-Q hysteresis loop analysis in karst catchment storm events, and what additional

90   information can bring the modeling of lateral flow Q and C. To answer these questions, we apply

91   the two-step approach on hourly records of Q and EC during storm events at 4 gauging stations

92   in two karst catchments in France, characterized by contrasting climate and karst area extension.

93   Results are interpreted in terms of water origin using PEW and EW contributions during storm

94   events. Finally, conceptual models are proposed, that summarize the main information obtained

95   with the combined approach, regarding spatio-temporal variability of flood processes.

96   2   Methodology

97   2.1   General methodology

98   To propose a conceptual model of flood water origin spatio-temporal variability, a two-

99   part methodology was applied. The parts correspond to two spatial scales: i) the nested

100   catchment scale considering the topographic catchment upstream a gauging station, and ii) the

101   reach scale considering the catchment delimited by two gauging stations. Both parts rely on

5

102 hourly Q and C data collection during storm events, the difference being that reach scale analysis

103 requires data from both inlet and outlet stations. To analyze temporal variability, the

104 methodology was applied on storm-events grouped by seasons. Figure 1 presents this general

105 methodology, from field measurement network and monitored variables to data processing.

106   At the nested catchment scale, C-Q loops are analyzed for each storm event according to

107 the methodology described in section 2.2. This analysis is performed at each monitoring station

108 of the hydrograph network and characterizes flood processes occurring in the whole upstream

109 topographic catchment. It is thus a lumped approach at the catchment scale, and successive

110 analyses towards the final outlet are interpreted in terms of flood process variability of nested

111 catchments. Even so, a more spatially discrete approach at the reach scale is necessary to refine

112 and spatialize this variability description.

113   At the reach scale, the hourly lateral flow discharge (Q_L) and concentration (C_L)

114 variations are simulated using the DWE inverse model, detailed in section 2.3, assuming that

115 exchanges are uniformly distributed along river reaches. Although this may not be the case in

116 karst systems, this approach allows a more spatialized investigation of the location of lateral

117 flows, which commonly lacks in C-Q studies. This reach-scale approach, consists in comparing

118 obtained mean C_L values to PEW and EW end-member C values. More details regarding

119 definitions of these end-members are given in section 3.3.

120

121 [Figure 1]

122

123   A season-based storm-event typology is proposed, which allows interpreting hydrological

124 response variability. Four seasons are defined, based on typical hydrological dynamics of the

6

125   study sites: low water table and first storm events in September and October, high precipitation

126   volume winter events from November to March, lower intensity events from April to May, and

127   occasional summer storm events from June to August. Finally, a conceptual model that

128   associates flood processes to different seasons and karst configurations is proposed, in addition

129   to a schematic representation of the spatial variability of water origin along river reaches.

2.2 Nested catchment scale approach: C-Q loop analysis

131   This section presents a C-Q loop classification that allows characterizing hysteresis loops

132   obtained from the monitoring of various physico-chemical parameters (concentration, turbidity,

133   EC, …). Evans and Davies (1998) proposed a 6-type classification of C-Q loops based on the

134   loop's general trend and its rotational direction. This classification was used in later C-Q studies

135   (Rose, 2003; Vaughan et al., 2017; Zhang et al., 2020). Building on Evans and Davies (1998),

136   we use a modified loop typology, enriched by the integration of a hysteresis index quantification

137   and the inclusion of non-hysteresis pathways. Similar 9-type classifications have been proposed

138   and shown to be relevant for C-Q relationship studies (Butturini et al., 2008; Heathwaite and

139   Bieroza, 2020). We calculated two indicators for loop classification: slope (s), obtained by

140   applying a linear regression to the C-Q values, and hysteresis index (HI).

141   The hysteresis index proposed by Lloyd et al. (2016) is used in this work. It provides

142   information on both the loop direction and its amplitude. Moreover, it considers the whole range

143   of discharge values and is calculated based on normalized Q and EC values, which facilitates

144   consistent inter-event and inter-site comparison. For a given storm event, Q and EC values are

145   normalized between 0 and 1, and at each 5% interval (i) of normalized Q, a local HI_i is

146   calculated following eq. 1:

147                                $$HI_i = EC_{nRi} - EC_{nFi}$$ (1)

148   Where EC_{nRi} and EC_{nFi} are normalized EC values at discharge interval i, taken on the

149   rising limb and falling limb of the loop, respectively. Figure 2 represents local HI_i values and the

150   slope value for an illustrative storm event. The mean of the 19 HI_i values (5% intervals,

151   recommended by Lloyd et al, 2016) is used as the final HI value. As a result, HI values range

152   from -1 to 1, absolute values near 0 and 1 corresponding to low and high hysteresis degrees,

153   respectively (similar versus contrasting rising and falling paths). Negative HI values indicate

154   anticlockwise loops whereas positive HI values indicate clockwise loops. Complex 8-shaped

155   loops show an HI value corresponding to their primary shape (i.e. the widest loop part with one

156   rotational direction).

157

158   [Figure 2]

159

8

160   Once threshold values are defined (values of slope and HI that delineate the classification

161   types), measure slope and HI make it possible to relate any storm event to one of the nine

162   categories of the classification presented in Figure 3, using its C-Q loop. The loop typology is

163   built on two-character names, the first corresponding to HI sign (and consequently to rotational

164   direction: C for clockwise, N for neutral and A for anticlockwise), and the second corresponding

165   to the slope sign (- for negative s, 0 for nil s, and + for positive s). This classification based on

166   Butturini et al. (2008) was adapted to the case of EC-Q in karst catchments.

167

168   In the case of karst areas, event water (EW) having a lower residence time than pre-event

169   water (PEW), its EC value is lower. Indeed, EC is a reliable proxy of bicarbonates concentration,

170   which is linked to limestone dissolution and thus residence time (Peyraube et al., 2019).

171   Therefore, we will use our EC-Q loop typology to determine patterns of successive contributions

172   to streamflow (PEW and EW), assuming the EC ranking is known.

173   Each loop type is linked to a specific pattern of successive contributions to streamflow,

174   based on the main findings in the literature of C-Q studies. Evans and Davies (1998) showed

175   that, in a two-component system, when the solute concentration of PEW is higher than that of

176   EW, anticlockwise C-Q loops indicate a dominant contribution of EW during the rising limb, and

177   a dominant contribution of PEW during the falling limb (scenario 1). On the other hand,

178   clockwise C-Q loops indicate a dominant PEW contribution during the rising limb and a

179   dominant EW contribution during the falling limb (scenario 2). This C-Q loop taxonomic

180   consistency was verified experimentally by Chanat et al. (2002), and was shown to be reliable

181   when concentration values of end-members are distinct enough, which is the case here as surface

9

182 runoff water and groundwater are compared (see values at end of section 3.3). Regarding the

183 specific case of EC-Q hysteresis, Toran and Reisch (2012) observed anticlockwise loops during

184 storm events at a karst spring discharge in Pennsylvania and verified that they were linked to

185 Scenario 1 based on Ca^{2+} and Mg^{2+} concentration monitoring. Rose et al. (2018) linked Scenario

186 2 to clockwise C-Q loops thanks to geogenic solute monitoring in a small USA catchment. In the

187 case of monitoring of solutes in which EW is enriched, such as NO_3^- from the organic horizon

188 (Evans et al., 1999; Huebsch et al., 2014), the rotational directions are reversed.

189   Based on previously described findings from the literature and in our case of EC

190 monitoring in a karst catchment where the PEW solute concentration is higher, our hypothesis is

191 that clockwise EC-Q loops correspond to PEW preceding EW and anticlockwise EC-Q loops

192 correspond to EW preceding PEW. This is particularly clear with loops that have slopes equal to

193 zero (C0 and A0 loops), rising and falling limbs showing EC values exclusively above or below

194 the initial value prior to a storm event. In the case of non-zero loop slopes, one limb may have

195 mixed water origins. A mixed water signature, in the case of karst systems where fast infiltration

196 can occur, may result from low residence time PEW recently stored in the karst (i.e., from

197 several days or weeks) or from EW infiltrating through preferential pathways and mixing with

198 highly mineralized PEW (i.e. several months or years old). Regarding non-hysteretic EC-Q

199 paths, both limbs have a similar water origin, this latter being inferred from the slope (a negative

200 slope indicating EW contribution whereas a positive slope indicating PEW contribution).

201   This methodology is applicable only when the initial EC value falls between the two end-

202 member EC values. This observation was systematically verified in the framework of this study

203 (the initial EC value always being higher than the EW end-member EC value in karst areas).

204 More information on end-member EC values is provided in section 3.3. On Figure 3 that presents

10

205   the nine loop types of our classification, a framework of interpretation of associated streamflow

206   contribution patterns is also proposed based on residence time, which is inferred from EC values.

207   Mixed water can be linked either to a mix of low and high residence time PEW or to a mix of

208   EW and high residence time PEW.

209

210   [Figure 3]

211

2.3 Reach-scale approach: lateral flow simulation

213   To investigate the origin of lateral inflows along river reaches (i.e. between two gauging

214   stations), we used the modeling approach proposed by Cholet et al. (2017) based on the diffusive

215   wave equation (DWE) and extended to the advection–diffusion equation (ADE). Both equations

216   are resolved using the Hayami analytical solution (1951) as proposed by Moussa (1996). We

217   provide in this section the key points of the approach. More details on this analytical approach

218   are provided in the Appendix.

219   Separate modeling of lateral discharge Q_L and mass flux M_L make it possible to assess

220   lateral solute concentration C_L by division, as shown in equation 2.

221   $$C_L = \frac{M_L}{Q_L}$$ (2)

222   Q_L is simulated using the solution of the inverse problem of the DWE and ADE,

223   assuming that lateral flow is uniformly distributed along the river reach (Moussa, 1996). M_L is

224   obtained by applying the DWE to mass flux, this latter being calculated as the product of Q_L and

225   C_L (equation 2). Assuming that total dissolved solids (TDS) consists mainly of conductive ionic

226   compounds, EC is proportional to the TDS concentration (noted C, in $g.m^{-3}$). Concentration C is

11

227 therefore calculated from EC, using a constant factor of 0.64, in accordance with values found in

228 the literature (Lloyd and Heathcote, 1985):

229 $$C = EC \cdot 0.64 \qquad (3)$$

230 Mass flux M is then calculated as the product of concentration C and discharge Q:

231 $$M = C \cdot Q \qquad (4)$$

232 Finally, the simulated lateral conductivity EC_L is calculated as the ratio of simulated

233 lateral mass flux M_L to simulated lateral discharge Q_L, divided by a factor of 0.64:

234 $$EC_L = \frac{M_L}{Q_L} \cdot \frac{1}{0.64} \qquad (5)$$

235 As some river reaches can show negative Q_L values, indicating lateral streamflow losses,

236 EC_L is calculated only for positive Q_L values. Indeed, negative Q_L values would lead to negative

237 EC_L values, which is impossible. EC_L variations thus make it possible to compare water origin

238 on successive streams within a catchment.

239

3 Study areas and data sets

3.1 Study areas

242 The previously described methodology was applied to two catchments in France, which

243 are partially to strongly karstified, and located in different geological and hydrometeorological

244 settings (figure 4). They are similar in size (~ 1000 km²) and both include four Q and EC

245 measurement stations.

246 The Loue River basin is located in the Jura Mountains. Its outcrops consist primarily of

247 extensively and homogeneously karstified Jurassic limestone and locally marl, making it a unary

12

248   karst basin. The Lison River is the major left bank Loue tributary and oth rivers start as a karst

249   spring. The Loue spring being partly fed by Doubs river losses that occur in the southeastern part

250   of the catchment (Charlier et al., 2014), it is not a typically unary karst basin. The term of unary

251   karst basin is used here as the allogenic recharge is also from a similar karstified area. The Loue

252   and Lison springs are among the largest karst springs in Europe (Chen et al., 2017), with mean

253   discharge of around 10 and 7 $m^3.s^{-1}$, respectively, and maximum peak flows of around 80 and 70

254    $m^3.s^{-1}$. Precipitation follows an elevation gradient; annual values range from 1600 mm on the

255   upstream catchment at elevations of 900 m (a.s.l) to 1450 mm at the outlet, at an elevation of

256   around 400 m (a.s.l).

257   The Cèze catchment is located in the eastern part of the Cévennes Mountains. It can be

258   characterized as a binary karst basin with upstream areas that consist of non-karst outcrops (i.e.

259   hard rocks) where mean yearly precipitation is 1500 mm and median and downstream areas

260   underlain by karst plateaus that receive precipitation of approximately 1000 mm/year. The

261   karstified portion is composed of early Cretaceous limestone (dark green, figure 54b) that is

262   mainly situated between the Tharaux and Laroque stations, and extends southward. More

263   information on exchanges between river streams and karst systems in this area can be found in

264   the work of Chapuis (2018).

265

266   [Figure 4]

267

13

3.2 Data sets

Detailed information on the data time series is available in the supplementary material. Temporal data used in this paper are:

- Hourly streamflow data, available from the French public streamflow database 'Banque Hydro' (http://www.hydro.eaufrance.fr).

- Hourly rainfall data, available from the Antilope database (Champeaux et al., 2011), a reanalysis produced by the French public meteorological service Météo France (http://www.meteofrance.fr/).

- Sub-hourly EC measurements for the Cèze river, recorded by the BRGM using Schlumberger CTD diver probes from July 2019 to July 2020. Similar data recorded using OTT MS5 probes within the QUARSTIC network (Charlier et al., 2018) for the Loue River, from January 2016 to January 2020.

As available data time series on the studied catchments are not of identical length and because of contrasted hydro-climatic contexts, 58 storm events were extracted for the Loue catchment, against 8 for the Cèze catchment. In the Loue catchment, storm events have a median precipitation depth of 58 mm (min: 10 mm and max: 136 mm) and a median peak flow value of 78 $m^3.s^{-1}$ (min: 2 $m^3.s^{-1}$ and max: 529 $m^3.s^{-1}$). In the Cèze catchment, storm events have a median precipitation depth of 65 mm (min: 30 mm and max: 180 mm) and a median peak flow value of 128 $m^3.s^{-1}$ (min: 20 $m^3.s^{-1}$ and max: 780 $m^3.s^{-1}$).

14

3.3 EC end-member values

289   For the Loue catchment, the PEW end-member EC is defined as the signal for water

290   having the longest residence time, thus having the highest EC value (at 550 $\mu S.cm^{-1}$) recorded

291   during the acquisition period at the spring monitoring stations (Ouhans and Nans, see figure 4a).

292   The Loue catchment EW end-member EC for surface runoff is defined at 250 $\mu S.cm^{-1}$, based on

293   values recorded on an intermittent stream on marly areas. For the Cèze catchment, the PEW end-

294   member is defined at 700 $\mu S.cm^{-1}$, based on highest values recorded at Cèze karst springs

295   monitoring stations (Chapuis, 2018). The Cèze catchment EW end-member EC for surface

296   runoff is defined at 75 $\mu S.cm^{-1}$, based on minimum values recorded during the acquisition period

297   at the upstream monitoring station (Tharaux, see figure 4b) which is only fed by non-karst areas.

298

299

300   # 4 Results

301   ## *4.1 EC-Q relationships at the catchment scale*

302   Figure 5 compares annual and event-based mean EC values for the Loue and Cèze

303   catchment stations. To obtain the mean EC value of all water flowing through stations, we

304   calculated the flow-weighted average of hourly EC..

305   For both annual and event-based EC, the four Loue stations show similar values, of

306   around 400 and 350 $\mu S.cm^{-1}$, respectively. This consistency across stations is probably linked to

307   the homogeneous presence of karst areas, leading to similar proportions of surface water and

308   groundwater contribution to streamflow. Event-based EC values are generally higher than annual

15

309   ones, indicating a dominant mobilization of pre-event highly mineralized water during storms,

310   likely groundwater, as the two downstream river stations (Vuillafans and Chenecey) show

311   similar responses to the two spring stations (Nans and Ouhans).

312   The Cèze catchment stations show a spatial variability pattern, with EC values increasing

313   from upstream to downstream and decreasing again at the most downstream station. Annual

314   values range from 180 $\mu S.cm^{-1}$ at Tharaux to 280 $\mu S.cm^{-1}$ at Laroque. Event-based EC values

315   follow the same trend, in relation to the local karst extension: the intermediate karst area located

316   between Tharaux and Laroque (see fig 5b) promoting highly mineralized water. Event-based EC

317   values are mostly lower than annual ones, showing a dominant stream dilution by low-

318   mineralization event water during storms, except at the Tharaux station.

319

320   [Figure 5]

321

322   Figure 6 shows two examples of recorded EC and Q variations for each study site (Loue:

323   a,b; Cèze: c,d), along with their corresponding EC-Q loops (see Figure 3 for classification).

324   These illustrative events were chosen as they are representative of the generally observed EC and

325   Q variations at each site. Regarding the Loue catchment, figure 6a shows a storm event

326   associated with an EC drop that takes place mostly after peak flow and leads to a C- loop type

327   indicating an event-water (EW) contribution that occurs mainly at the end of peak flow and

328   during recession. Figure 6b shows that other storm events on the Loue catchment are associated

329   with an EC increase, indicating pre-event water (PEW) mobilization. On the pictured storm-

330   event, EC variations are quite similar to Q variations, leading to a flatter EC-Q loop.

16

331   Nevertheless, EC values are slightly higher on the falling limb, leading to an identifiable A+ loop

332   type.

333   Regarding the Cèze catchment, figure 6c illustrates a storm event associated with an EC

334   decrease, indicating dilution by event water and leading to a C- loop type, as shown in figure 6a.

335   Finally, figure 6d represents a storm event with strongly anticorrelated EC and Q variations

336   during both rising and falling limbs, leading to a non-hysteretic N- loop type.

337

338   [Figure 6]

339

340   Figure 7a and 7b show the seasonal slope value distribution in the Loue and Cèze

341   catchments, respectively. All stations in the Loue catchment exhibit a similar pattern of seasonal

342   variation, with negative or low slopes in winter (November to March) and spring (April to May),

343   and positive values in summer (June to August) and fall (September to October). This shows that

344   storm events in winter and spring are primarily characterized by an EW dilution while storm

345   events in summer and fall are mainly characterized by a PEW mobilization. From June to

346   October, the variability of slope is higher. Moreover, slope values are generally lower at the

347   Nans and Chenecey stations than at the others.

348   Regarding the Cèze catchments, slope values are mostly negative all year long, except for

349   a few winter storm events at the Tharaux and Bagnols stations, indicating the dominant dilution

350   by low-mineralization EW.

351   Figures 7c and 7d show the HI value distribution following seasons for the Loue and

352   Cèze catchments, respectively. Both catchments are subject to strong seasonal influence, even

353   though the patterns are different. The Loue catchment stations show mostly positive HI values in

17

354 winter and spring, and negative HI values in summer and fall. This corresponds to clockwise and

355 anticlockwise EC-Q loops, respectively. Analyzed in line with slope values (see Figure 3), these

356 loops show that in winter and spring, the dominant contribution is EW, with a minor contribution

357 of PEW at the beginning of storm events. In summer and fall, the dominant contribution is PEW,

358 with a minor contribution of EW or slightly mineralized PEW at the beginning of storm events.

359   Contrary to the Loue catchment, Cèze catchment stations show mostly positive HI values

360 in fall, corresponding to clockwise loops. During this season, slope values are mostly negative,

361 showing that the dominant contribution is EW, associated with a minor contribution of PEW at

362 the beginning of storm events. In winter, HI values are near zero, corresponding to non-

363 hysteretic EC-Q paths (similar EC values for a given discharge amount on rising and falling

364 limbs). During this season, slope values are primarily negative, showing that the dominant

365 contribution is EW on both limbs.

366

367 [Figure 7]

368

369   Table 1 summarizes the main EC-Q loop types on the Loue and Cèze catchments for all

370 seasons. In the Loue catchment, predominantly clockwise EC-Q hysteresis loops (C- and C0)

371 occur during winter and spring, while anticlockwise loops (A0 and A+) dominate in summer and

372 fall. Conversely, the Cèze catchment stations show mostly non-hysteretic behavior in winter (N-

373 loops) and show clockwise loops (C- and C0) in summer and fall.

374

375

376

18

377   *Table 1: Commonly occurring EC-Q loop types on the Loue and Cèze catchments*

Catchment	Station	Sep-Oct	Nov-Mar	Apr-May	Jun-Aug
Loue	Nans	A+	C-	C-	N0
	Ouhans	A+	C-	C+	N+
	Vuillafans	A+	C0	C+	A+
	Chenecey	A0/A+	C0	N0	A+
Cèze	Tharaux	C-	N-	-	C+
	Montclus	~	N-	-	C0
	Laroque	C-	N-	-	C-
	Bagnols	C0	~	-	C-

378   - = no storm event and ~ = no clear dominant behavior

379

380   As these results provide information for nested catchments, their analysis on successive

381   stations can highlight spatial variability in flood water origin towards the final outlet. Even

382   though EC-Q loop types are quite homogeneous for the four stations for a given catchment, some

383   differences are observed. Regarding Loue catchment, the Nans and Chenecey stations have

384   particularly low slope values. Indeed, except for summer events, most of their EC-Q loops have

385   slopes lower than 1 (figure 7a). This indicates a greater EW effect at the Nans-Chenecey and

386   Vuillafans-Chenecey (downstream reaches, see figure 4a). This is also the case regarding Cèze

387   catchment, where lower slopes are characterized for Montclus. Because each nested catchment

388   incorporates the upstream previous one, these intra-site trends are not totally straightforward and

389   can hardly be quantified.

390

391   ## 4.2 EC of reach-scale lateral flow

392   Figure 8 shows examples of observed Q and EC at input (Q_{IN}) and output (Q_{OUT}) stations,

393   as well as simulated lateral Q_L and EC_L for the Loue (a, b) and Cèze (c, d) catchments. On the

19

394   Loue catchment example (left), EC_L, EC_{IN}, and EC_{OUT} are similar with values ranging between

395   350 and 400 $\mu S.cm^{-1}$, meaning that the mass flux remains quite proportional to discharge rate.

396   On the Cèze catchment example (right), as Q_O is slightly delayed near peak flow, simulated Q_L

397   shows a brief period of loss (negative values). The corresponding EC_L is not calculated for

398   outflows, as it would lead to negative values. EC_L for inflows values are around 250 $\mu S.cm{-1}$,

399   slightly higher than measured input and output EC (200 $\mu S.cm{-1}$), indicating PEW mobilization.

400   EC_L values decrease at the end of the period, indicating the decreased contribution of PEW.

401

402   [Figure 8]

403

404   Figure 9 shows the distribution of simulated lateral flow EC on the Loue and Cèze River

405   reaches. EC_L mean values are calculated around the peak of lateral flow ($Q_L > 0.75Q_{L,max}$), so as

406   to obtain a value that is representative of the major amount of lateral water inflow. Values of EW

407   and PEW EC end members are also plotted on the graphs. As the simulation of EC_L values is

408   made using the DWE, it requires a simple reach with one input and one output. For this reason,

409   the Nans-Chenecey reach is not represented (see the river confluence on figure 4a).

410   Regarding the Loue catchment (figure 9a), the upstream reach (Ouhans-Vuillafans)

411   shows EC_L values mainly above 400 $\mu S.cm^{-1}$, except for some winter storm events. Lateral water

412   inflows are thus of mixed origin. On the downstream reach (Vuillafans-Chenecey), EC_L values

413   are lower, mostly less than 400 $\mu S.cm^{-1}$. This reach-scale approach provides more precise and

414   discretized information of the streamflow contribution variability within catchment, and is

415   consistent with the lower slope values measured at the Chenecey station in figure 7, indicating a

416   higher EW signature. This can be explained by a higher contribution of either surface runoff

20

417   downstream the canyon area (open valleys in the downstream parts of the catchment) or EW

418   from fast infiltration pathways, or both. It is also noticeable that EC_L distribution are more

419   spreaded on the downstream reach, probably due to more intense or frequent water mixing.

420   On the Cèze catchment (figure 9b), EC_L values span from 100 to 300 $\mu S.cm^{-1}$ on the two

421   median reaches (Tharaux-Montclus and Montclus-Laroque), whereas most EC_L values on the

422   downstream reach (Laroque-Bagnols) are lower (around 100 $\mu S.cm^{-1}$). This pattern is consistent

423   with its karst outcrop location, located between Tharaux and Laroque (figure 4b) and the EC

424   river measurement (figure 5b).

425

426   [Figure 9]

427

5   Discussion

5.1   Conceptual model of flood water origin and process variability

431   Figures 10a to 10d show the main hysteresis loop types, associated hydrographs, and the

432   scheme of flood water origin and processes for the Loue (unary) and Cèze (binary) karst

433   catchments, for two contrasted periods in the hydrological cycle. Figures 10e and 10f represent,

434   within each catchment, the reach-scale variability of streamflow contribution. The conceptual

435   model provides key insights into the influence of seasons and karst configuration on flood

436   processes.

21

437   In the Loue unary karst catchment, mainly C- type EC-Q loops are observed from

438   November to May (figure 10a), corresponding to a dominant contribution sequence of 1) mix of

439   EW and PEW and 2) EW. This sequence can be explained by a two-step process involving 1)

440   during the rising limb, EW infiltrating into karst drains and pushing PEW into the stream,

441   associated with EW from fast infiltration or surface runoff, and 2) during the falling limb, EW

442   that infiltrated into karst drains reaching the stream, associated with surface runoff. From June to

443   October (figure 10b), mainly A+ type loops are observed, corresponding to a dominant

444   contribution sequence of 1) mixed water and 2) PEW. This can be explained by a lower degree

445   of saturation in the karst system, reducing surface runoff contribution, and showing a purely

446   piston-type flow leaching the PEW initially stored in the aquifer.

447   In the Cèze binary karst catchment N- type loops are the most common between

448   November and May (figure 10c), corresponding to a dominant contribution of EW during both

449   rising and falling limbs. This pattern is explained by the lower storage capacity of smaller karst

450   units compared to the Loue catchment. The high karst system saturation level leads to a blocked

451   infiltration and promotes increased EW surface runoff. From June to October (figure 10d), C-

452   EC-Q loops are the most common type observed, corresponding to a dominant contribution

453   sequence of 1) mixed water and 2) EW. At this period of the year, the karst system is less

454   saturated, which reduces the surface runoff signature associated with blocked infiltration, and

455   shows PEW reaching streams by piston-type flow, associated with the EW influence, leading to

456   similar processes as described for figure 10a.

457

458   [Figure 10]

459

    22

460   The surface runoff contribution to streamflow is less important in the Loue catchment

461   compared to the Cèze one, as seen in previous sections. This fact is explained by the catchment's

462   morphology, which is for the unary catchment a typical configuration of plateaus and canyons

463   that promotes higher rainfall infiltration and groundwater contribution to surface flows (Le

464   Mesnil et al., 2020). This type of surface water-groundwater interaction is promoted in other

465   catchments made up of plateaus and canyons, where stream losses and/or lateral gains from

466   springs occur according to hydrological conditions (Bailly-Comte et al., 2009; De Waele, 2010;

467   Charlier et al., 2019). Our results confirm this behavior, which results in increased EC values and

468   positive slope values of the hysteresis EC-Q loops. Because the saturation level of the karst

469   aquifer also plays an important role on the mobilisation of PEW and EW, its low or high storage

470   capacity can affect flood process variability. To interpret surface runoff contributions in the Cèze

471   catchment, we need to refer to the two main types of flooding that are documented in the

472   literature for karst areas: 1) infiltration excess runoff due to the low infiltration capacity of the

473   karst medium (Maréchal et al. 2008), and 2) backflooding following infiltration with a

474   simultaneous rapid rise of the aquifer water level due to a limited saturation capacity of the

475   conduit network (Lopez-Chicano et al. 2002; Bonacci et al. 2006; Bailly-Comte et al. 2008). The

476   first process is linked to rainfall intensities, that are high under the specific Mediterranean

477   climate of the Cèze river. The second one is more dependent on the storage capacity of the karst

478   aquifer, which is small for the Cèze (compared to high elevation plateaux for the Loue).

479   Superimposed on seasonal influence, physiographical factors also control intra-site

480   variability of flood processes and catchment's response to storm events. Indeed, the extension of

481   karst areas and topographic relief can both affect the water origin of streamflow. In the Loue

482   catchment, the reach-scale lateral flow simulation (section 4.2) highlights a water origin spatial

483   variability characterized by an increasing EW contribution to storm events in the downstream

484   direction. This increased EW contribution is explained by the typical plateau-and-canyon

485   morphology of the upstream portion grading into open valleys downstream, resulting in higher

486   surface runoff.

487   The Cèze catchment, as shown in figure 4b, is characterized by a binary karst, that is, a

488   delineated karstified area downstream of hard-rock headwater zones. Le Mesnil et al. (2020;

489   2021) showed that this specific karst location plays a role in the annual water budget, as well as

490   in the flood pattern. In this study, EC monitoring shows that it also controls flood water origin, as

491   illustrated by EC values increasing on the karst zone (figure 5b). This spatial variability within

492   the Cèze catchment was detected by our reach-scale approach of lateral flow simulation, EC_L

493   values being increasing in the median reaches where the karst crops out. This approach shows

494   that water being mobilized during floods has a higher PEW signature in this zone. Figures 10e

495   and 10f provide a sketch of the main features of streamflow contribution variability within each

496   study site.

5.2 Pros and cons of the C-Q relationship analysis approach

498   Our approach makes it possible to differentiate storm events in which PEW may or may

499   not be mobilized, thanks to EC monitoring. This approach is a suitable for assessing the role of

500   groundwater in flooding, which in many cases is supposed to be mobilized without being

501   quantified (e.g. Ascott et al., 2017). For example, applying this methodology in the context of

502   groundwater-induced flooding in chalk regions (Finch et al., 2004; Pinault et al., 2005) or

503   lowland karst areas (Jerome Morrissey et al., 2020) may be of great value, as well as for rivers

504   that show complex and variable exchanges with underlying aquifers (Bailly-Comte et al., 2009;

24

505   Charlier at al., 2015; 2019). Indeed, a better understanding of the groundwater role in flooding is

506   essential for efficient management of flood hazards in karst areas. Several authors develop tools

507   in this purpose (Gill et al., 2013; Mayaud et al., 2019). A recent study of Le Mesnil et al. (2021)

508   based on 108 gauging stations shows in the one hand that karst promotes generally peak-flow

509   attenuation due partly to higher water infiltration from rivers, and in the other hand that the

510   hydrological response is highly site-specific. The development of approaches investigating water

511   origin as proposed in this paper gives interesting perspective to explore such variability and to

512   facilitate their modeling, for example using semi-distributed models. Moreover, the proposed

513   approach was kept generic enough to be applicable to a variety of contexts. This section provides

514   a brief summary of the main features of this two-step methodology, what can be expected from

515   its application, and what it requires.

516   The nested-catchment scale approach is integrative, as it provides information on the

517   topographic catchment from a particular monitoring station to its upstream limit. Even so,

518   analysis of results at successive monitoring stations provides information on water origin and

519   flood process variability along the river. Loop slope and hysteresis index (Lloyd et al., 2016) of

520   C-Q paths can be used to classify storm events through the use of a loop typology adapted and

521   enriched from the work of Evans and Davies (1998). Other hysteresis classifications have been

522   proposed previously for karst areas, but include less types and do not allow to represent all storm

523   processes: e.g. the 3-type T-C curve classification by Fournier et al. (2007). Our classification

524   can be used with a variety of parameters (EC, concentrations, turbidity, …) involving different

525   processes. In the framework of this study, it allowed determining flood water origin seasonal

526   patterns on the two studied catchments. This first approach requires only concentration and

527   discharge datasets at a consistent resolution (hourly for storm-event analysis, possibly wider time

528   steps for other purposes) for one outlet station. It can thus be easily implemented at little cost

529   (especially for EC continuous monitoring).

530   This nested-catchment scale approach involves some limitations. First, the concentration

531   ranking of potential contributing end-members must be known to make a consistent

532   interpretation of the involved processes. Then, no more than two end members can be

533   differentiated when monitoring one concentration variable. Finally, in the specific case of karst

534   systems, the approach cannot always properly differentiate between EW that originates from

535   surface runoff and EW that originates from fast infiltration through underground karst conduits.

536   Indeed, localized infiltration in sinkholes for instance can be quick enough to keep water

537   chemistry unchanged due to residence times of few hours/days. In this case, other techniques

538   such as signal processing or baseflow separation might be necessary to figure out

539   comprehensively which flood processes are involved, as well as analysis of alternative physico-

540   chemical data such as organic carbon to track infiltration water with short residence time (Pronk

541   et al., 2009; Charlier et al., 2012). Some anomalous EC variations can also be witnessed during

542   high-flow periods, as groundwater catchments expand and incorporate areas of different typical

543   EC values (Ravbar et al., 2011).

544   The reach-scale approach is based on the inverse modeling approach (Moussa, 1996)

545   using the diffusive wave equation. It allows simulating Q and C variations in lateral exchange

546   flow of a river reach (Cholet et al., 2017). Analyzed along with end-member EC values, this

547   analysis highlighted the increasing contribution of EW towards the downstream end of the Loue

548   catchment and the major PEW contribution in the karst zone in the median area of the Cèze

549   catchment. This analytical approach is very convenient as it allows investigating spatial

26

550 variability of lateral exchanges without conducting extensive field work such as tracing tests

551 (e.g. Covino et al., 2011).

552   This second part is more data-dependent, as it requires similar datasets than the first part,

553 but recorded at both inlet and outlet stations. Moreover, the approximate EC value of each end

554 member must be known to interpret the results in terms of water origin mixing. Though, this

555 reach-scale approach provides more precise and discretized information on spatial variability of

556 streamflow contributions within catchments.

557 # 6 Conclusions

558   We applied a C-Q relationship analysis approach, using hysteresis loop classification at

559 the nested catchment scale combined with lateral flow and concentration simulation at the reach

560 scale. In the framework of this study, this combined method made it possible to establish a

561 seasonal conceptual model of water origin during storm events for two contrasted karst

562 catchments and to infer its spatial variability at the scale of the monitoring network.

563   Analysis of EC-Q hysteresis loops highlighted a flood water origin pattern, with

564 successive contributions of pre-event water (PEW) and event water (EW) according to karst type

565 (unary vs. binary) and seasonality (low flow periods vs. high flow periods). Simulation of lateral

566 exchange flows led to a more detailed analysis of the water origin, spatializing it at the reach

567 scale. This analysis highlighted the decreasing contribution of PEW in favor of EW as the

568 canyons and plateaus that the Loue flows through grade into open valleys, the significant PEW

569 effect on the karst area of the Cèze catchment, and the role of the aquifer saturation state in flood

570 response.

27

571   Our results show that, in karst context the nested catchment scale analysis of C-Q

572   hysteresis loops provides information on seasonality of flood processes, and trends of intra-

573   catchment variability. We also show that the reach scale lateral flow simulation provides a

574   quantifiable information on intra-catchment variability of streamflow contributions. The tested

575   approach is innovative and particularly suitable for partly karstified catchments, as it is semi-

576   distributed and uses EC measurements which are a reliable proxy of water residence time. Our

577   results are encouraging to apply these complementary methodologies to a variety of sites of

578   differing geology, with additional investigational purposes, such as water resource management

579   and modeling. Indeed, such approach providing discretized information on flood processes

580   within catchments could help refining lumped model structure, or facilitate the use of semi-

581   distributed models. Some perspectives are identified, as coupling the monitoring of multiple

582   solutes, making it possible to differentiate additional end members.

Author contribution

584   RM and JBC were involved in conceptualization, funding acquisition, and supervision.

585   MLM gathered the data and designed the methodology with the help of JBC, RM, and YC.

586   MLM prepared the manuscript with the help of all co-authors.

587

28

592   Hourly streamflow data were gathered from the "Banque hydro" database using a script

593   available at http://doi.org/10.5281/zenodo.3744183. EC datasets of the Loue catchment were

594   monitored within the QUARSTIC network funded by the BRGM, the Doubs Department, and

595   the Rhône Mediterranean Corsica Water Agency, and the NUTRI-Karst project founded by

596   BRGM and Rhône Mediterranean Corsica water agency.

597   The authors declare that they have no known competing financial interests or personal

598   relationships that could have appeared to influence the work reported in this paper.

599

References

601   Anderson, S. P., Dietrich, W. E., Torres, R., Montgomery, D. R., & Loague, K. (1997).

602   Concentration-discharge relationships in runoff from a steep, unchanneled catchment. Water

603   Resources Research, 33(1), 211–225. https://doi.org/10.1029/96WR02715

604   Ascott, M. J., Marchant, B. P., Macdonald, D., McKenzie, A. A., & Bloomfield, J. P.

605   (2017). Improved understanding of spatio-temporal controls on regional scale groundwater

606   flooding using hydrograph analysis and impulse response functions. Hydrological Processes,

607   31(25), 4586–4599. https://doi.org/10.1002/hyp.11380

608   Baeumer, B., Benson, D. A., Meerschaert, M. M., & Wheatcraft, S. W. (2001).

609   Subordinated advection-dispersion equation for contaminant transport. Water Resources

610   Research, 37(6), 1543–1550. https://doi.org/10.1029/2000WR900409

611   Bailly-Comte, V., Jourde, H., Roesch, A., Pistre, S., & Batiot-Guilhe, C. (2008). Time

612   series analyses for Karst/River interactions assessment: Case of the Coulazou river (southern

613   France). Journal of Hydrology, 349(1–2), 98–114. https://doi.org/10.1016/j.jhydrol.2007.10.028

29

614   Bailly-Comte, V., Jourde, H., & Pistre, S. (2009). Conceptualization and classification of

615   groundwater–surface water hydrodynamic interactions in karst watersheds: Case of the karst

616   watershed of the Coulazou River (Southern France). Journal of Hydrology, 376(3–4), 456–462.

617   https://doi.org/10.1016/j.jhydrol.2009.07.053

618   Bakalowicz, M. (2005). Karst groundwater: a challenge for new resources. Hydrogeology

619   Journal, 13(1), 148–160. https://doi.org/10.1007/s10040-004-0402-9

620   Bonacci, O., Ljubenkov, I., & Roje-Bonacci, T. (2006). Karst flash floods: an example

621   from the Dinaric karst (Croatia). Natural Hazards and Earth System Science, 6(2), 195–203.

622   Burns, D. A., McDonnell, J. J., Hooper, R. P., Peters, N. E., Freer, J. E., Kendall, C., &

623   Beven, K. (2001). Quantifying contributions to storm runoff through end-member mixing

624   analysis and hydrologic measurements at the Panola Mountain Research Watershed (Georgia,

625   USA). Hydrological Processes, 15(10), 1903–1924. https://doi.org/10.1002/hyp.246

626   Butturini, A., Alvarez, M., Bernal, S., Vazquez, E., & Sabater, F. (2008). Diversity and

627   temporal sequences of forms of DOC and NO3-discharge responses in an intermittent stream:

628   Predictable or random succession?. Journal of Geophysical Research: Biogeosciences, 113(G3).

629   Champeaux, J.-L., Laurantin, O., Mercier, B., Mounier, F., Lassegues, P., & Tabary, P.

630   (2011). Quantitative precipitation estimations using rain gauges and radar networks: inventory

631   and prospects at Meteo-France, 11.

632   Chanat, J. G., Rice, K. C., & Hornberger, G. M. (2002). Consistency of patterns in

633   concentration-discharge plots. Water Resources Research, 38(8), 22-1-22–10.

634   https://doi.org/10.1029/2001WR000971

635   Chapuis, H. (2018). Caractérisation, évaluation, modélisation des échanges entre

636   aquifères karstiques et rivières - Application à la Cèze (Gard, France), 467.

30

637   Charlier, J.-B., Bertrand, C., & Mudry, J. (2012). Conceptual hydrogeological model of

638   flow and transport of dissolved organic carbon in a small Jura karst system. Journal of

639   Hydrology, 460–461, 52–64. https://doi.org/10.1016/j.jhydrol.2012.06.043

640   Charlier J.-B., Desprats J.-F., Ladouche B. (2014). Appui au SCHAPI 2014 – Module 1 –

641   Rôle et contribution des eaux souterraines d'origine karstique dans les crues de la Loue à

642   Chenecey-Buillon, BRGM/RP-63844-FR report, 109p. https://infoterre.brgm.fr/rapports/RP-

643   63844-FR.pdf (accessed February 2021)

644   Charlier, J.-B., Moussa, R., Bailly-Comte, V., Danneville, L., Desprats, J.-F., Ladouche,

645   B., & Marchandise, A. (2015). Use of a flood-routing model to assess lateral flows in a karstic

646   stream: implications to the hydrogeological functioning of the Grands Causses area (Tarn River,

647   Southern France). Environmental Earth Sciences, 74(12), 7605–7616.

648   https://doi.org/10.1007/s12665-015-4704-0

649   Charlier J.-B., Vallet A., G. Hévin, F. Moiroux (2018) – Projet QUARSTIC : QUAlité

650   des eaux et Réseau de Surveillance des rIvières Comtoises. BRGM/RP-68315-FR report, 165p.

651   http://infoterre.brgm.fr/rapports/RP-68315-FR.pdf (accessed February 2021)

652   Charlier, J., Moussa, R., David, P., & Desprats, J. (2019). Quantifying peakflow

653   attenuation/amplification in a karst river using the diffusive wave model with lateral flow.

654   Hydrological Processes. https://doi.org/10.1002/hyp.13472

655   Chen, Z., Auler, A. S., Bakalowicz, M., Drew, D., Griger, F., Hartmann, J., et al. (2017).

656   The World Karst Aquifer Mapping project: concept, mapping procedure and map of Europe.

657   Hydrogeology Journal, 25(3), 771–785. https://doi.org/10.1007/s10040-016-1519-3

658   Cholet, C., Charlier, J.-B., Moussa, R., Steinmann, M., & Denimal, S. (2017). Assessing

659   lateral flows and solute transport during floods in a conduit-flow-dominated karst system using
31

660   the inverse problem for the advection–diffusion equation. Hydrology and Earth System Sciences,

661   21(7), 3635–3653. https://doi.org/10.5194/hess-21-3635-2017

662   Cimorelli, L., Cozzolino, L., Della Morte, R., & Pianese, D. (2014). Analytical solutions

663   of the linearized parabolic wave accounting for downstream boundary condition and uniform

664   lateral inflows. Advances in Water Resources, 63, 57–76.

665   https://doi.org/10.1016/j.advwatres.2013.11.003

666   Covino, T., McGlynn, B., & Mallard, J. (2011). Stream-groundwater exchange and

667   hydrologic turnover at the network scale. Water Resources Research, 47(12).

668   https://doi.org/10.1029/2011WR010942

669   De Waele, J., Martina, M. L. V., Sanna, L., Cabras, S., & Cossu, Q. A. (2010). Flash

670   flood hydrology in karstic terrain: Flumineddu Canyon, central-east Sardinia. Geomorphology,

671   120(3–4), 162–173. https://doi.org/10.1016/j.geomorph.2010.03.021

672   Doctor, D. H., Alexander, E. C., Petrič, M., Kogovšek, J., Urbanc, J., Lojen, S., &

673   Stichler, W. (2006). Quantification of karst aquifer discharge components during storm events

674   through end-member mixing analysis using natural chemistry and stable isotopes as tracers.

675   Hydrogeology Journal, 14(7), 1171–1191. https://doi.org/10.1007/s10040-006-0031-6

676   Evans, C., Davies, T. D., & Murdoch, P. S. (1999). Component flow processes at four

677   streams in the Catskill Mountains, New York, analysed using episodic concentration/discharge

678   relationships. Hydrological Processes, 13(4), 563–575. https://doi.org/10.1002/(SICI)1099-

679   1085(199903)13:4<563::AID-HYP711>3.0.CO;2-N

680   Evans, Christopher, & Davies, T. D. (1998). Causes of concentration/discharge hysteresis

681   and its potential as a tool for analysis of episode hydrochemistry. Water Resources Research,

682   34(1), 129–137. https://doi.org/10.1029/97WR01881

32

683   Finch, J. W., Bradford, R. B., & Hudson, J. A. (2004). The spatial distribution of

684   groundwater flooding in a chalk catchment in southern England. Hydrological Processes, 18(5),

685   959–971. https://doi.org/10.1002/hyp.1340

686   Fournier, M., Massei, N., Bakalowicz, M., Dussart-Baptista, L., Rodet, J., & Dupont, J. P.

687   (2007). Using turbidity dynamics and geochemical variability as a tool for understanding the

688   behavior and vulnerability of a karst aquifer. Hydrogeology Journal, 15(4), 689–704.

689   https://doi.org/10.1007/s10040-006-0116-2

690   Gill, L. W., Naughton, O., & Johnston, P. M. (2013). Modeling a network of turloughs in

691   lowland karst: Modeling a Network of Turloughs in Lowland Karst. Water Resources Research,

692   49(6), 3487–3503. https://doi.org/10.1002/wrcr.20299

693   Goldscheider, N., Chen, Z., Auler, A. S., Bakalowicz, M., Broda, S., Drew, D., et al.

694   (2020). Global distribution of carbonate rocks and karst water resources. *Hydrogeology Journal*,

695   *28*(5), 1661–1677. https://doi.org/10.1007/s10040-020-02139-5

696   Hartmann, A., Jasechko, S., Gleeson, T., Wada, Y., Andreo, B., Barberá, J. A., et al.

697   (2021). Risk of groundwater contamination widely underestimated because of fast flow into

698   aquifers. *Proceedings of the National Academy of Sciences*, *118*(20).

699   https://doi.org/10.1073/pnas.2024492118

700   Hauns, M., Jeannin, P.-Y., & Atteia, O. (2001). Dispersion, retardation and scale effect in

701   tracer breakthrough curves in karst conduits. Journal of Hydrology, 241(3–4), 177–193.

702   https://doi.org/10.1016/S0022-1694(00)00366-8

703   Heathwaite, A. L., & Bieroza, M. (2021). Fingerprinting hydrological and

704   biogeochemical drivers of freshwater quality. Hydrological Processes, 35(1), e13973.

33

705   Hess, J. W., & White, W. B. (1988). Storm response of the karstic carbonate aquifer of

706 southcentral Kentucky. Journal of Hydrology, 99(3–4), 235–252. https://doi.org/10.1016/0022-

707 1694(88)90051-0

708   House, W. A., & Warwick, M. S. (1998). Hysteresis of the solute concentration/discharge

709 relationship in rivers during storms. Water Research, 32(8), 2279–2290.

710 https://doi.org/10.1016/S0043-1354(97)00473-9

711   Huebsch, M., Fenton, O., Horan, B., Hennessy, D., Richards, K. G., Jordan, P.,

712 Goldscheider, N., Butscher, C., and Blum, P. (2014). Mobilisation or dilution? Nitrate response

713 of karst springs to high rainfall events, Hydrol. Earth Syst. Sci., 18, 4423–4435,

714 https://doi.org/10.5194/hess-18-4423-2014

715   Jerome Morrissey, P., McCormack, T., Naughton, O., Meredith Johnston, P., & William

716 Gill, L. (2020). Modelling groundwater flooding in a lowland karst catchment. *Journal of

717 Hydrology*, *580*, 124361. https://doi.org/10.1016/j.jhydrol.2019.124361

718   Knapp, J. L. A., von Freyberg, J., Studer, B., Kiewiet, L., & Kirchner, J. W. (2020).

719 Concentration&#8211;discharge relationships vary among hydrological events, reflecting

720 differences in event characteristics. Hydrology and Earth System Sciences, 24(5), 2561–2576.

721 https://doi.org/10.5194/hess-24-2561-2020

722   Lambán, L. J., Jódar, J., Custodio, E., Soler, A., Sapriza, G., & Soto, R. (2015). Isotopic

723 and hydrogeochemical characterization of high-altitude karst aquifers in complex geological

724 settings. The Ordesa and Monte Perdido National Park (Northern Spain) case study. Science of

725 The Total Environment, 506–507, 466–479. https://doi.org/10.1016/j.scitotenv.2014.11.030

726   Le Mesnil, M., Charlier, J.-B., Moussa, R., Caballero, Y., & Dörfliger, N. (2020).

727 Interbasin groundwater flow: Characterization, role of karst areas, impact on annual water

728   balance and flood processes. Journal of Hydrology, 585, 124583.

729   https://doi.org/10.1016/j.jhydrol.2020.124583

730   Le Mesnil, M., Moussa, R., Charlier, J.-B., Caballero, Y. (2021). Impact of karst areas on

731   runoff generation, lateral flow and interbasin groundwater flow at the storm-event timescale.

732   Hydrol. Earth Syst. Sci. 25, 1259–1282. https://doi.org/10.5194/hess-25-1259-2021

733   Liu, Z., Li, Q., Sun, H., & Wang, J. (2007). Seasonal, diurnal and storm-scale

734   hydrochemical variations of typical epikarst springs in subtropical karst areas of SW China: Soil

735   CO_2 and dilution effects. Journal of Hydrology, 337(1–2), 207–223.

736   https://doi.org/10.1016/j.jhydrol.2007.01.034

737   Lloyd, C. E. M., Freer, J. E., Johnes, P. J., & Collins, A. L. (2016). Technical Note:

738   Testing an improved index for analysing storm discharge–concentration hysteresis. Hydrology

739   and Earth System Sciences, 20(2), 625–632. https://doi.org/10.5194/hess-20-625-2016

740   Lloyd, J. W., & Heathcote, J. A. (1985). Natural inorganic hydrochemistry in relation to

741   ground water. Retrieved from https://www.osti.gov/biblio/6026514

742   López-Chicano, M., Calvache, M. L., Martín-Rosales, W., & Gisbert, J. (2002).

743   Conditioning factors in flooding of karstic poljes—the case of the Zafarraya polje (South Spain).

744   CATENA, 49(4), 331–352. https://doi.org/10.1016/S0341-8162(02)00053-X

745   Luhmann, A. J., Covington, M. D., Alexander, S. C., Chai, S. Y., Schwartz, B. F.,

746   Groten, J. T., & Alexander, E. C. (2012). Comparing conservative and nonconservative tracers in

747   karst and using them to estimate flow path geometry. Journal of Hydrology, 448–449, 201–211.

748   https://doi.org/10.1016/j.jhydrol.2012.04.044

749   Mallard, J., McGlynn, B., & Covino, T. (2014). Lateral inflows, stream-groundwater

750   exchange, and network geometry influence stream water composition. Water Resources

751   Research, 50(6), 4603–4623. https://doi.org/10.1002/2013WR014944

752   Maréchal, J. C., Ladouche, B., & Dörfliger, N. (2008). Karst flash flooding in a

753   Mediterranean karst, the example of Fontaine de Nîmes. Engineering Geology, 99(3–4), 138–

754   146. https://doi.org/10.1016/j.enggeo.2007.11.013

755   Massei, N., Mahler, B. J., Bakalowicz, M., Fournier, M., & Dupont, J. P. (2007).

756   Quantitative Interpretation of Specific Conductance Frequency Distributions in Karst. Ground

757   Water, 45(3), 288–293. https://doi.org/10.1111/j.1745-6584.2006.00291.x

758   Mayaud, C., Gabrovšek, F., Blatnik, M., Kogovšek, B., Petrič, M., & Ravbar, N. (2019).

759   Understanding flooding in poljes: A modelling perspective. *Journal of Hydrology*, *575*, 874–889.

760   https://doi.org/10.1016/j.jhydrol.2019.04.092

761   Moussa, R. (1996). Analytical Hayami solution for the diffusive wave flood routing

762   problem with lateral inflow. Hydrological Processes, 10(9), 1209–1227.

763   https://doi.org/10.1002/(SICI)1099-1085(199609)10:9<1209::AID-HYP380>3.0.CO;2-2

764   Moussa, R., & Bocquillon, C. (1996). Criteria for the choice of flood-routing methods in

765   natural channels. Journal of Hydrology, 186(1–4), 1–30. https://doi.org/10.1016/S0022-

766   1694(96)03045-4

767   Moussa, R., & Bocquillon, C. (2009). On the use of the diffusive wave for modelling

768   extreme flood events with overbank flow in the floodplain. Journal of Hydrology, 374(1–2),

769   116–135. https://doi.org/10.1016/j.jhydrol.2009.06.006

770   Moussa, R., & Majdalani, S. (2019). Evaluating lateral flow in an experimental channel

771 using the diffusive wave inverse problem. Advances in Water Resources, 127, 120–133.

772 https://doi.org/10.1016/j.advwatres.2019.03.009

773   Neira, J. M. T., Tallec, G., Andreassian, V., & Mouchel, J. M. (2020). A combined

774 mixing model for high-frequency concentration–discharge relationships. Journal of Hydrology,

775 591, 125559.

776   Peyraube, N., Lastennet, R., Denis, A., Minvielle, S., Houillon, N., Lorette, G., et al.

777 (2019). SIc–Abacus: An in–situ tool for estimating SIc and Pco2 in the context of carbonate

778 karst. Journal of Hydrology, 568, 891–903. https://doi.org/10.1016/j.jhydrol.2018.11.042

779   Pinault, J.-L., Amraoui, N., & Golaz, C. (2005). Groundwater-induced flooding in

780 macropore-dominated hydrological system in the context of climate changes. Water Resources

781 Research, 41(5). https://doi.org/10.1029/2004WR003169

782   Pronk, M., Goldscheider, N., Zopfi, J., & Zwahlen, F. (2009). Percolation and Particle

783 Transport in the Unsaturated Zone of a Karst Aquifer. Ground Water, 47(3), 361–369.

784 https://doi.org/10.1111/j.1745-6584.2008.00509.x

785   Ravbar, N., Engelhardt, I., & Goldscheider, N. (2011). Anomalous behaviour of specific

786 electrical conductivity at a karst spring induced by variable catchment boundaries: the case of the

787 Podstenjšek spring, Slovenia. Hydrological Processes, 25(13), 2130-2140.

788   Ribolzi, O., Andrieux, P., Valles, V., Bouzigues, R., Bariac, T., & Voltz, M. (2000).

789 Contribution of groundwater and overland ̄ows to storm ̄ow generation in a cultivated

790 Mediterranean catchment. Quanti®cation by natural chemical tracing. Journal of Hydrology, 17.

791   Rose, L. A., Karwan, D. L., & Godsey, S. E. (2018). Concentration-discharge

792 relationships describe solute and sediment mobilization, reaction, and transport at event and

793   longer timescales. Hydrological Processes, 32(18), 2829–2844.

794   https://doi.org/10.1002/hyp.13235

795   Rose, S. (2003). Comparative solute–discharge hysteresis analysis for an urbanized and a

796   'control basin' in the Georgia (USA) Piedmont. Journal of Hydrology, 284(1–4), 45–56.

797   https://doi.org/10.1016/j.jhydrol.2003.07.001

798   Runkel, R. L. (1996). Solution of the Advection-Dispersion Equation: Continuous Load

799   of Finite Duration. Journal of Environmental Engineering, 122(9), 830–832.

800   https://doi.org/10.1061/(ASCE)0733-9372(1996)122:9(830)

801   Singh, V. P. (2002). Is hydrology kinematic? Hydrological Processes, 16(3), 667–716.

802   https://doi.org/10.1002/hyp.306

803   Todini, E. (1996). The ARNO rainfall—runoff model. Journal of Hydrology, 175(1–4),

804   339–382. https://doi.org/10.1016/S0022-1694(96)80016-3

805   Toran, L., & Reisch, C. E. (2012). Using Stormwater Hysteresis to Characterize Karst

806   Spring Discharge. Ground Water, no-no. https://doi.org/10.1111/j.1745-6584.2012.00984.x

807   Tritz, S., Guinot, V., & Jourde, H. (2011). Modelling the behaviour of a karst system

808   catchment using non-linear hysteretic conceptual model. Journal of Hydrology, 397(3–4), 250–

809   262. https://doi.org/10.1016/j.jhydrol.2010.12.001

810   Vaughan, M. C. H., Bowden, W. B., Shanley, J. B., Vermilyea, A., Sleeper, R., Gold, A.

811   J., et al. (2017). High-frequency dissolved organic carbon and nitrate measurements reveal

812   differences in storm hysteresis and loading in relation to land cover and seasonality. Water

813   Resources Research, 53(7), 5345–5363. https://doi.org/10.1002/2017WR020491

814   Vidal, J.-P., Martin, E., Franchistéguy, L., Baillon, M., & Soubeyroux, J.-M. (2010). A

815   50-year high-resolution atmospheric reanalysis over France with the Safran system. International

816   Journal of Climatology, 30(11), 1627–1644. https://doi.org/10.1002/joc.2003

817   Zhang, R., Chen, X., Zhang, Z., & Soulsby, C. (2020). Using hysteretic behaviour and

818   hydrograph classification to identify hydrological function across the "hillslope–depression–

819   stream" continuum in a karst catchment. Hydrological Processes, 34(16), 3464–3480.

820   https://doi.org/10.1002/hyp.13793

821

Appendix: Hayami analytical resolution of DWE and ADE

Diffusive wave equation

824   An inverse modelling approach is adopted for simulating lateral flow between two

825   gauging stations. This approach simulates the lateral flow Q_L, based on measurements from two

826   gauging stations Q_I and Q_O.

827   The diffusive wave equation (DWE), accounting for lateral flow, is an approximation of

828   the St-Venant equation that can be written as:

829    $$\frac{\partial Q}{\partial t} + c(Q)\left[\frac{\partial Q}{\partial x} - q\right] - D(Q)\left[\frac{\partial^2 Q}{\partial x^2} - \frac{\partial q}{\partial x}\right] = 0 \qquad (A1)$$

830   where x [L] is the length along the channel, t [T] is the time, and celerity $c(Q)$ [LT^{-1}] and

831   diffusivity $D(Q)$[L^2T^{-1}] are functions of the discharge Q [L^3T^{-1}]. The term $q(x,t)$ [L^2T^{-1}]

832   represents the lateral flow distribution. The lateral hydrograph $Q_L(t)$ is given by:

833    $$Q_L(t) = \int_0^l q(x,t)dx \qquad (A2)$$

834   with l [L] the channel length.

39

835   Moussa (1996) extended the solution of the DWE under Hayami's hypotheses (semi-

836   infinite channel, c(Q) and D(Q) constant) to the case where lateral flow is uniformly distributed

837   along the channel. Let I(t) and O(t) be the inlet flow minus baseflow and the outlet flow minus

838   baseflow, respectively:

839        $O(t) = \varphi(t) + [I(t) - \varphi(t)] * K(t)$ (A3)

840   with K(t) the Hayami Kernel function defined as:

841        $K(t) = \dfrac{l}{2(\pi D)^{1/2}} \dfrac{e^{\left[\frac{Cl}{4D}\left(2 - \frac{l}{Ct} - \frac{Ct}{l}\right)\right]}}{t^{3/2}}$ (A4)

842   and

843        $\varphi(t) = \frac{c}{l} \int_0^t [Q_L(\theta) - Q_L(0)] d\theta$ (A5)

844   **The inverse problem**

845   Under Hayami's conditions and assuming that lateral flow is uniformly distributed along

846   the channel, Moussa (1996) proposed a solution of the inverse problem; this enables evaluation

847   of the temporal distribution of lateral flow $Q_L(t)$ over the channel reach by knowing I(t) and O(t).

848   Knowing c, D and l, the lateral flow can be calculated using the following procedure:

849        $L(t) = O(t) - I(t) * K(t)$ (A6)

850        $K^i(t) = K * K * \ldots * K$ (i times)   (A7)

851        $\varphi(t) = L(t) + L(t) \sum_{i=1}^{\infty} K^i(t)$ (A8)

852   and finally the lateral flow $Q_{L,c}(t)$

853        $Q_{L,c}(t) = Q_L(0) + \frac{l}{c} \frac{d\varphi}{dt}$ (A9)

854   The DWE equation has two free parameters, namely celerity c (m.s^{-1}) and diffusivity D

855   (m².s^{-1}) of the flood wave. Sensitivity analysis of the DWE to the two parameters is largely

856   available in the literature, showing that it is more sensitive to parameter c than D (Moussa and

857   Bocquillon, 1996; Cholet al., 2017; Charlier et al., 2019). Therefore, c is assumed equal to time

858   delay between peak discharges of Q_I and Q_O, and D is fixed in accordance with stream

859   characterization proposed by Todini (1996). The DWE solution was validated experimentally

860   under controlled conditions (Moussa and Majdalani, 2019), and has been implemented on natural

861   karst catchments (Charlier et al., 2015, 2019; Cholet et al., 2017).

862   The lateral mass fluxes M_L simulation by the ADE is done using the same analytical

863   solution than DWE, as under some hypotheses, the physical equations of both the DWE and the

864   ADE can lead to similar mathematical expressions. M_L is simulated using M_I and M_O.

41

Figure 1: Framework of the general methodology at the scales of nested catchments and river reaches. Spatial scales: topographic catchment vs. river reach. Monitored data: discharge (Q: Q_I at Inlet in light blue and Q_O at Outlet in dark blue) and electrical conductivity (EC: EC_I at I in light orange and EC_O at O in dark orange) during a storm event. Data processing: EC-Q hysteresis loop at the outlet O characterized by its slope (s) and hysteresis index (HI) versus inverse modelling of lateral Q_L and EC_L using the diffusive wave equation with Q_I, Q_O, EC_I and EC_O. PEW: Pre-Event Water; EW: Event Water.

Figure 2: Calculation of local HI_i indexes on an illustrative storm event (Chenecey, Jura, France, 18 September 2016).

Figure 3: EC-Q loop classification, adapted from Evans and Davies (1998), and corresponding streamflow contributions (PEW: pre-event water, EW: event water) in the case of catchments where EC is positively corelated to water residence time (e.g. karst areas), and initial EC is superior to EC value of EW end-member.

Figure 4: Location of gauging stations and river network in the studied catchments. Background: geological map. Karst outcrops are located on limestone areas .

Figure 5: Boxplots of mean EC values during storm events and corresponding annual values (circles) for Loue catchment (a) and Cèze catchment (b).
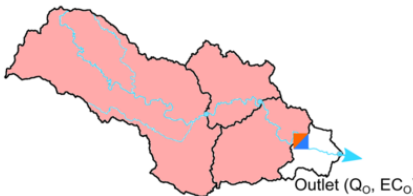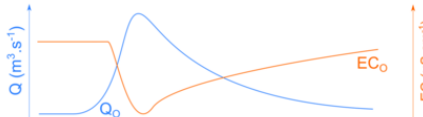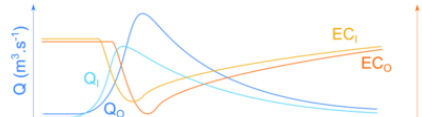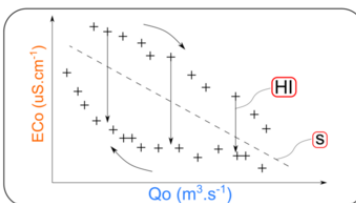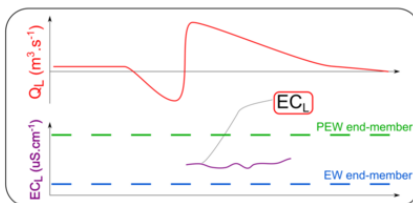
Figure 6: Examples of EC and Q variations recorded during storm events, with associated EC-Q loops and classifications. Slopes are expressed in $\mu S.cm^{-1}.m^{-3}.s$. HI is dimensionless. a: Nans (Loue), 14 March 2017; b: Ouhans (Loue), 3 June 2017; c: Montclus (Cèze), 20 October 2019; d: Laroque (Cèze), 22 November 2019.

Figure 7: Distribution of slope (a, b) and HI (c, d) values for the Loue (a, c) and Cèze (b, d) catchments, grouped by season. Black crosses indicate no available data.

Figure 8: Variations of input, output and lateral simulated discharge (a, c) and electrical conductivity (c, d). Example on the Loue catchment Ouhans-Vuillafans reach, March 2017 (left) and on the Cèze catchment Tharaux-Montclus reach, October 2019 (right).

Figure 9: Distribution of simulated lateral flow EC on Loue (a) and Cèze (b) reaches, mean values calculated around the peak of lateral inflow, with pre-event water (PEW) and event-water (EW) EC end-member values in dashed lines. From left to right, plotted reaches are from upstream to downstream.

Figure 10: Conceptual model of main flood processes and water origin seasonality in the Loue catchment (a and b) and the Cèze catchment (c and d), with hysteresis loop types, associated schematic hydrographs and main patterns of spatial variability (e and f). Dark blue: event water, green: pre-event water, light blue: total streamflow. Bottom triangles describe dominant water origin spatial variability from headwaters to outlet.

	Nested catchment scale approach	Reach scale approach
Spatial scale	Outlet (Q_O, EC_O) *Topographic catchment*	Inlet (Q_I, EC_I) Outlet (Q_O, EC_O) *River reach*
Monitored data	Q ($m^3.s^{-1}$) — EC ($\mu S.cm^{-1}$) EC_O Q_O *Outlet Q & EC*	Q ($m^3.s^{-1}$) — EC ($\mu S.cm^{-1}$) EC_I EC_O Q_I Q_O *Inlet and outlet Q & EC*
Data processing	EC_O ($\mu S.cm^{-1}$) vs Q_O ($m^3.s^{-1}$) HI, S *EC-Q loop analysis*	Q_L ($m^3.s^{-1}$) EC_L EC_L ($\mu S.cm^{-1}$) PEW end-member EW end-member *Lateral EC simulation*

Loue unary karst catchment (a)

Cèze binary karst catchment (b)

Chenecey

Vuillafans

Ouhans
Loue spr.

Nans
Lison spr.

N

0   10   20
Km

Tharaux

Montclus

Laroque

Bagnols

N

0   10   20
Km

(a)
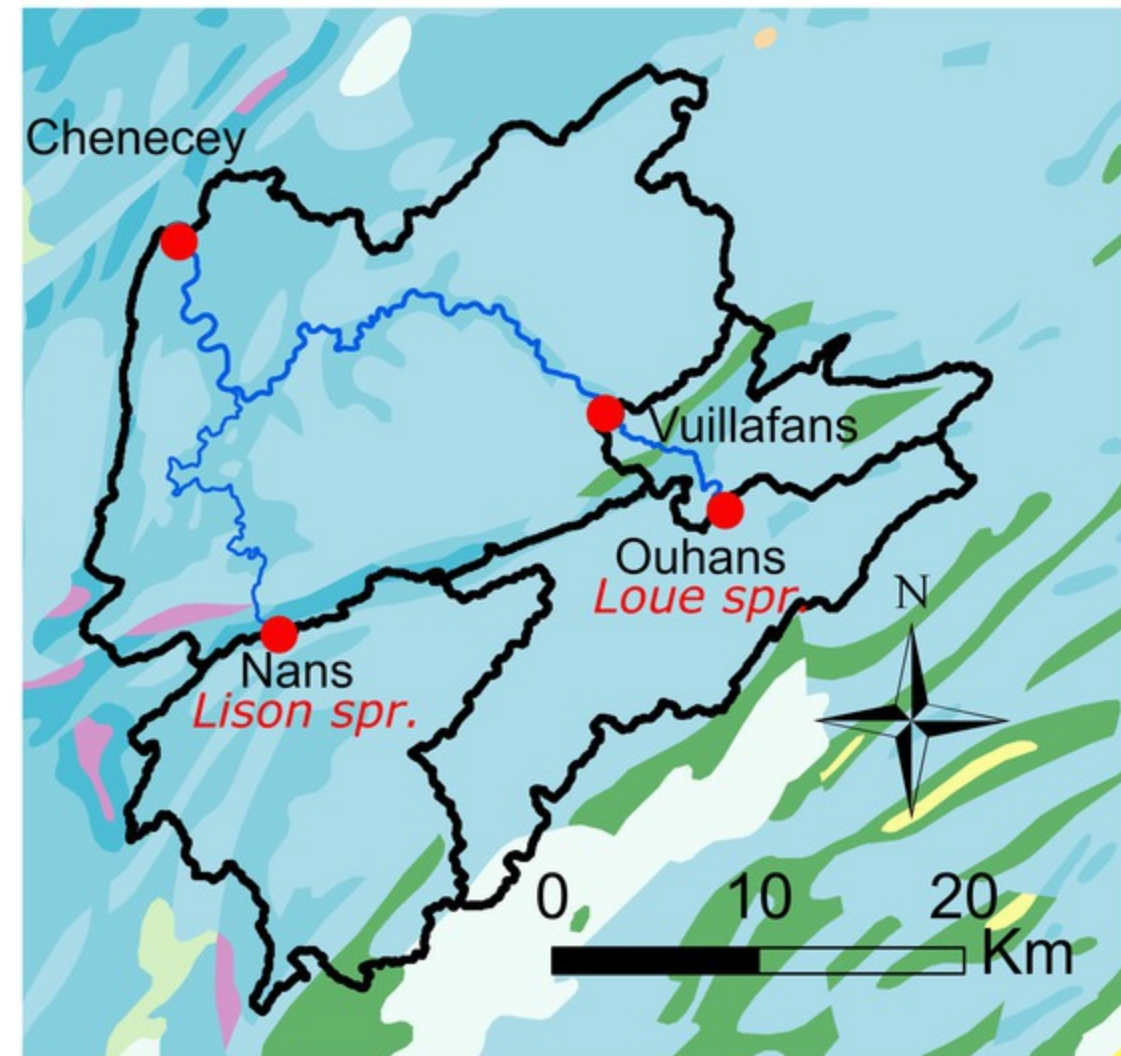
(b)
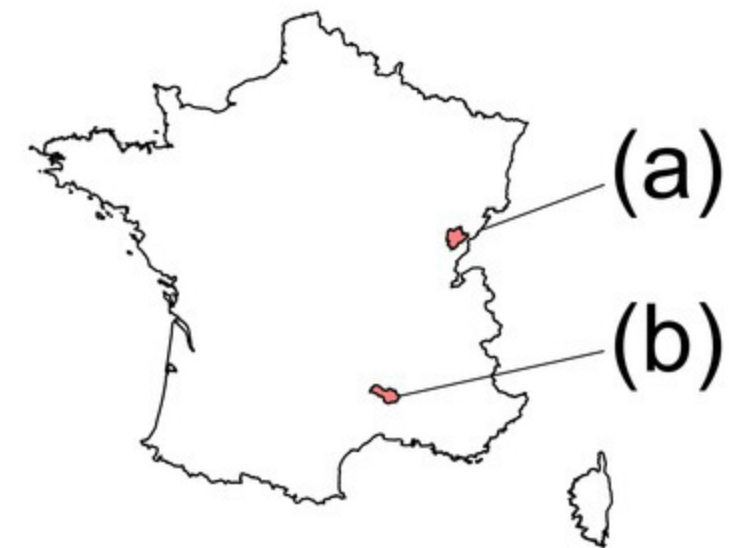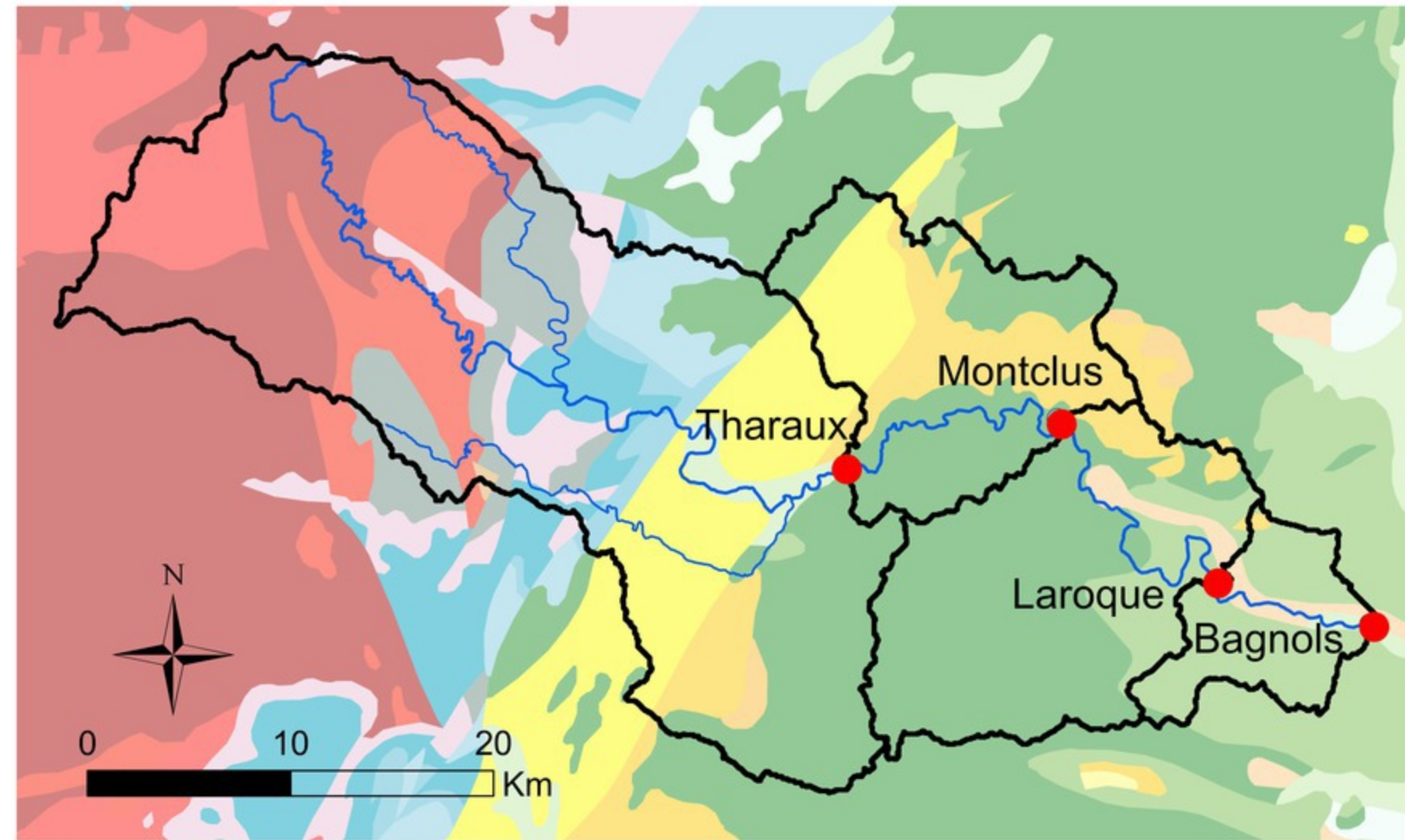
Main geological units

Paleogene limestones and sandstones

Cretaceous limestones

Jurassic limestones

Hard-rock formations

Loue (a)

Cèze (b)

Slope, Loue (a) — Nans, Ouhans, Vuillafans, Chenecey

Slope, Cèze (b) — Tharaux, Montclus, Laroque, Bagnols

HI, Loue (c) — Nans, Ouhans, Vuillafans, Chenecey

HI, Cèze (d) — Tharaux, Montclus, Laroque, Bagnols
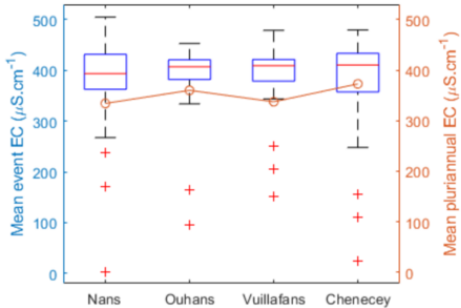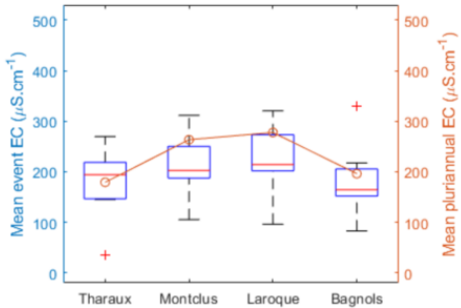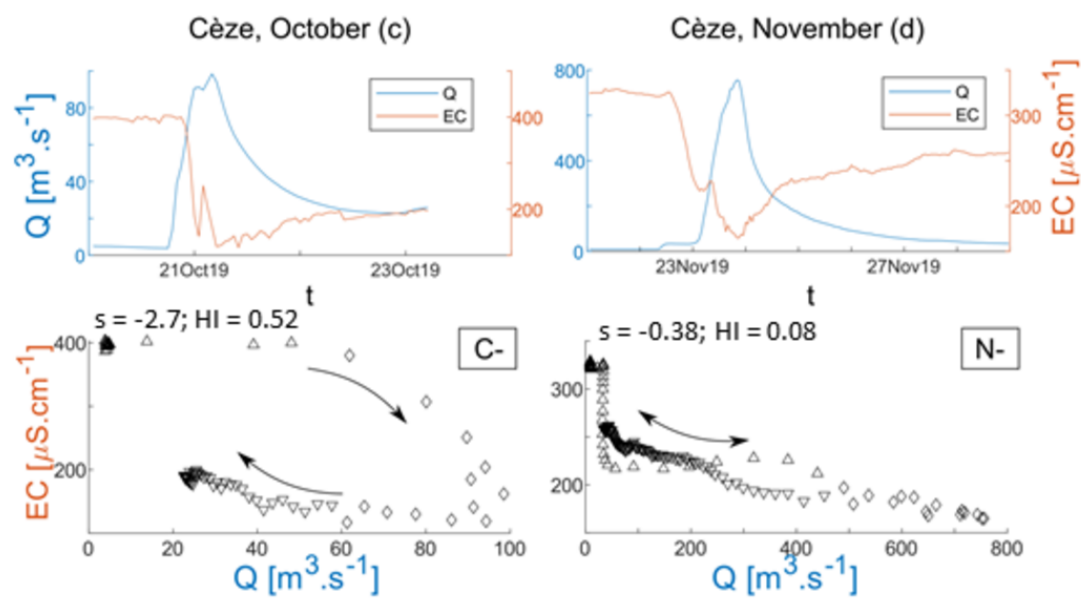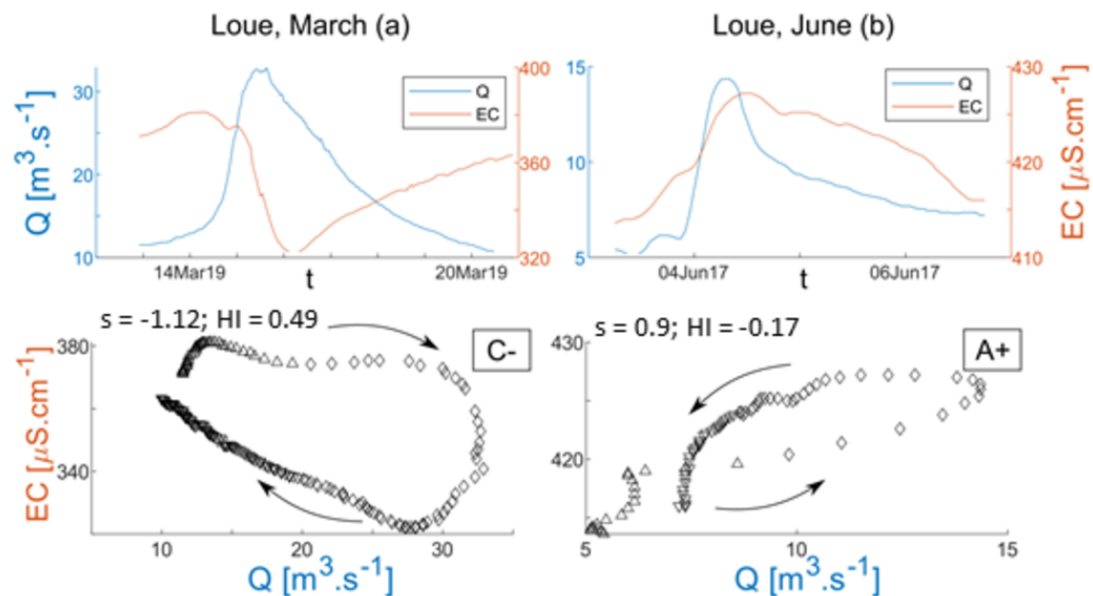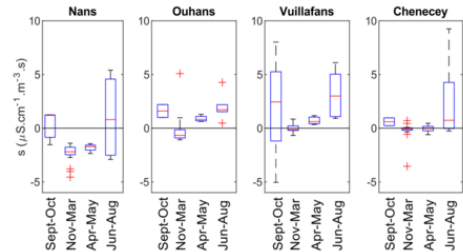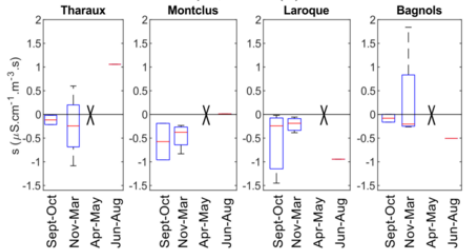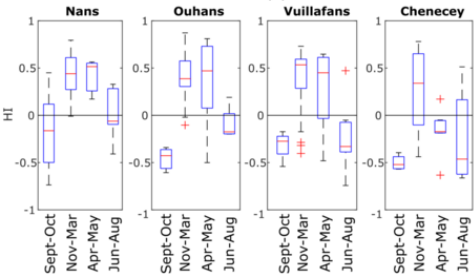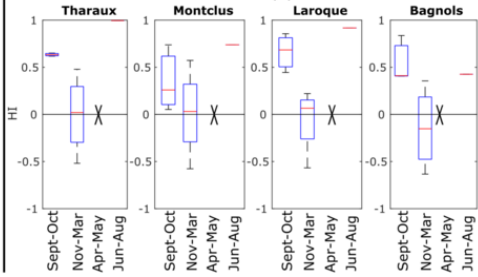
Loue: Ouhans - Vuillafans, 09 Mar 2017

(a) (b)

Cèze: Tharaux - Montclus, 24 Oct 2019

(c) (d)

Loue reaches (a)

Upstream → *Downstream*

Ouhans - Vuillafans | Vuillafans - Chenecey

Cèze reaches (b)

Upstream → *Downstream*

Tharaux - Montclus | Montclus - Laroque | Laroque - Bagnols
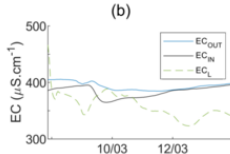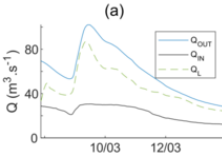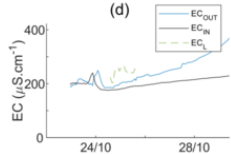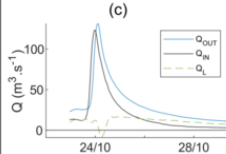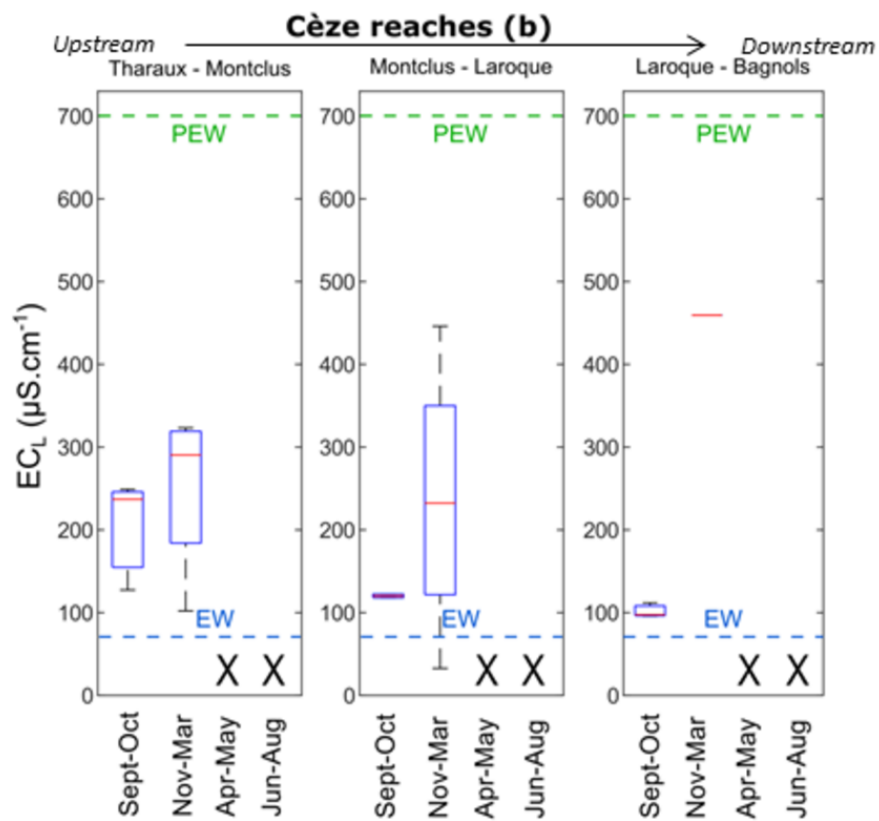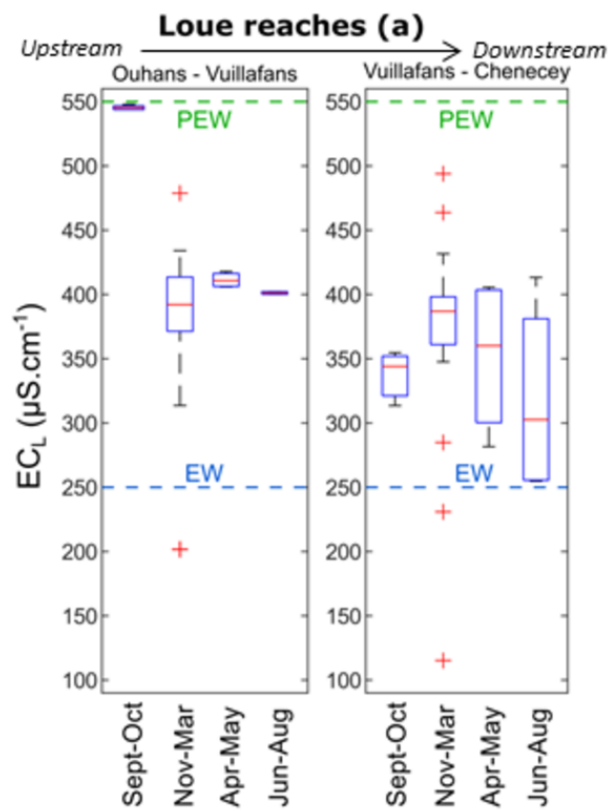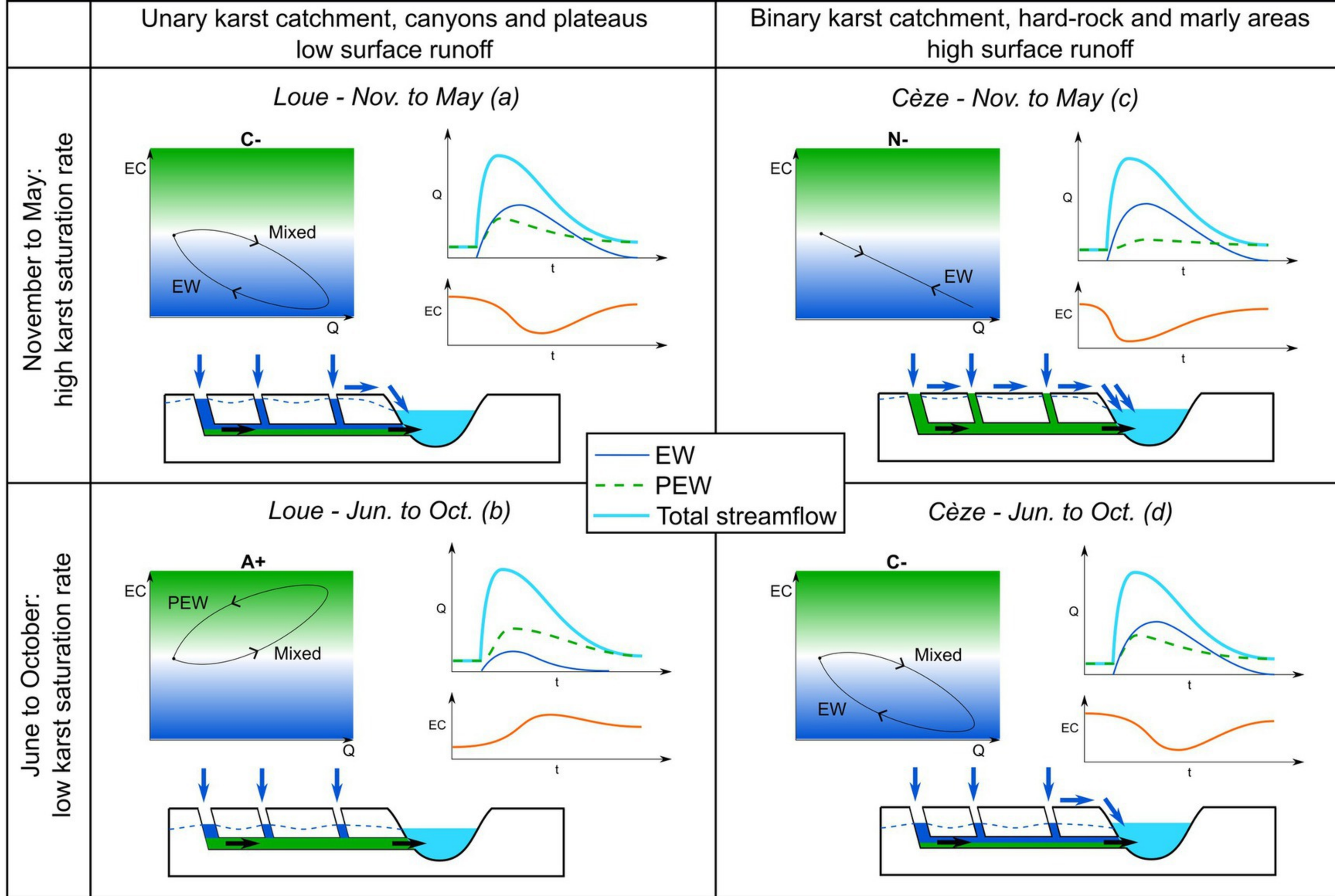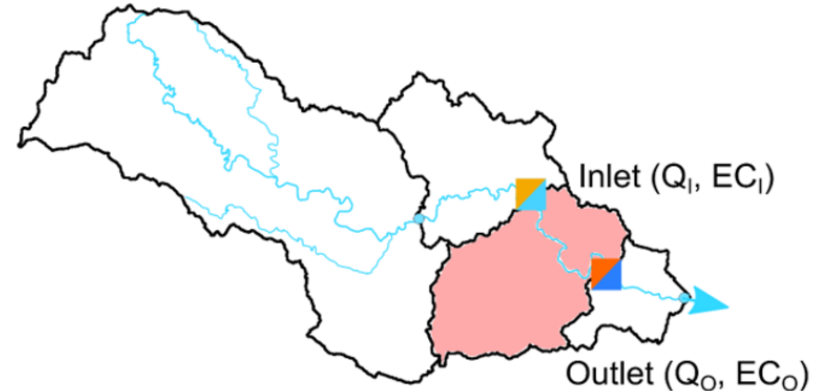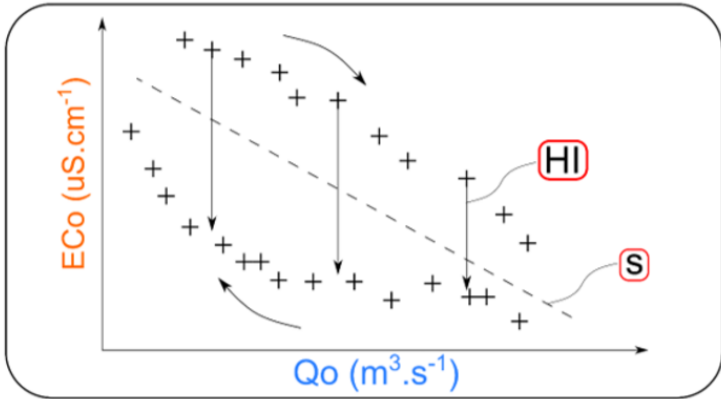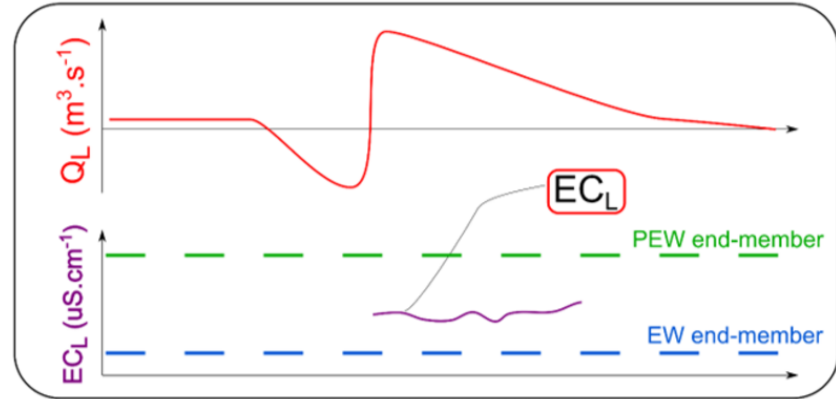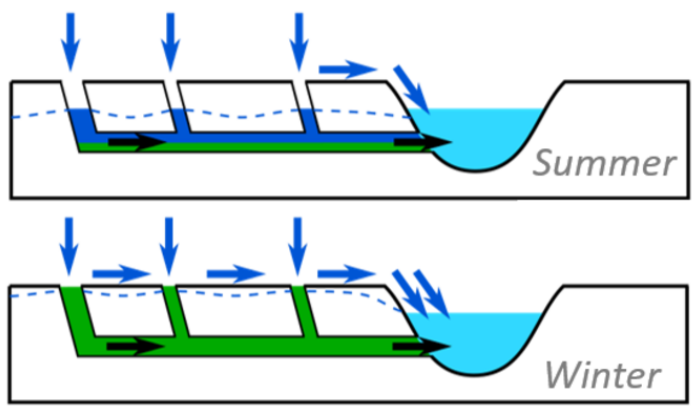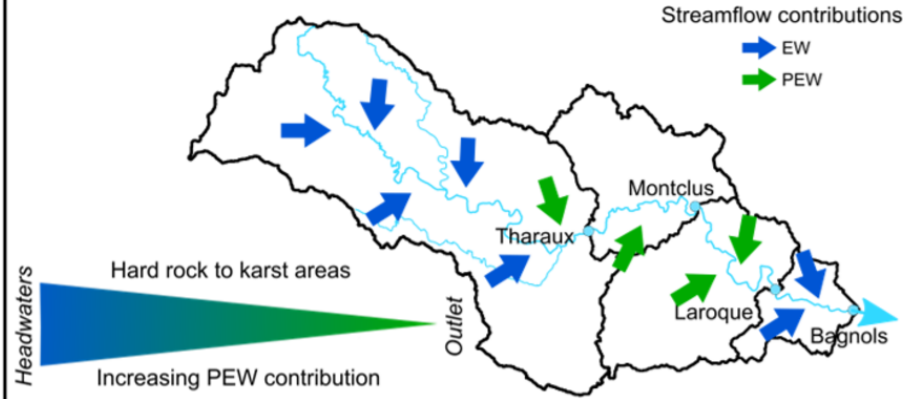
	Nested catchment scale approach	Reach scale approach
Spatial scale	*Topographic catchment*	*River reach*
Methodology	*EC-Q loop analysis*	*Lateral EC simulation*
Results	*Flood process seasonality*	*Intra-catchment water origin variability*